



# Experimental investigation of low-NO<sub>x</sub> H<sub>2</sub> combustion using simultaneous Raman and LIF spectroscopy

Z. Al Hadi<sup>1</sup>, S. Basnet<sup>1</sup>, S. Marragou<sup>1</sup>, P. Sharma<sup>1</sup>, T. Schuller<sup>3,4</sup>, T.F. Guiberti<sup>1,2</sup> and G. Magnotti<sup>1,2,\*</sup>

<sup>1</sup>Clean Energy Research Platform (CERP), King Abdullah University of Science and Technology (KAUST), Thuwal, 23955-6900, Saudi Arabia

<sup>2</sup>Mechanical Engineering Program, Physical Science and Engineering Division, King Abdullah University of Science and Technology

<sup>3</sup>Institut de Mécanique des Fluides de Toulouse, IMFT, Université de Toulouse, CNRS, Toulouse, France

<sup>4</sup>Institut Universitaire de France (IUF)

## I. Abstract

The global push toward decarbonization has positioned hydrogen as a key contender for clean energy applications. This study explores low-NO<sub>x</sub> hydrogen/air combustion in a lifted flame configuration using simultaneous 1D Raman and OH-LIF spectroscopy. High resolution measurements of temperature and species concentrations (H<sub>2</sub>, O<sub>2</sub>, and OH) provide crucial information on the structure of the flame and the stabilization mechanisms within a dual-swirl burner. The results reveal distinct inner and outer reaction fronts, each exhibiting unique combustion behaviors due to differences in gas composition, temperature, turbulence levels, and strain rates. The study focuses on the dynamics of the edge flame at the base of the outer reaction front, where air and hydrogen progressively mix along the flow axis. Detailed analysis of flow structure, flame dynamics, and properties at key locations highlights the interplay between flow and combustion processes. These findings provide a unique experimental data set for understanding the fundamental characteristics of swirled H<sub>2</sub> flames, validating numerical models, and guiding the development of optimized low-NO<sub>x</sub> H<sub>2</sub> combustion systems.

## II. Introduction

The concept of a hydrogen economy, first introduced by John Bockris in 1970 [1], envisions a future energy scenario in which hydrogen, produced from renewable sources, serves as a primary, carbon-free energy carrier for transportation, heating, and power generation. Although currently most hydrogen is produced from steam methane reforming, as the share of renewable energy increases, green hydrogen from water electrolysis will become economically viable. Research is needed in improving understanding of hydrogen combustion, to accelerate rapid adoption in power generation, industrial processing, and heavy-duty transportation sectors, once green hydrogen becomes widely available. In this context, retrofitting existing combustion technologies offers a viable pathway to facilitate the adoption of hydrogen. Conventional gas turbines with swirl burners require significant modifications to accommodate hydrogen injection safely and efficiently. To address these challenges, a new generation of coaxial burners with a swirled hydrogen stream has been developed [2]. The last iteration of this concept facilitates stabilization of turbulent hydrogen-air flames while mitigating issues such as flashback, burner overheating, and elevated NO<sub>x</sub> emissions. The concept leverages a central circulation zone (CRZ) [3] filled with burnt gases to aerodynamically stabilize the flames, enabling safe operation away from burner components. The dual-swirl burner configuration enhances mixing by creating interacting swirl flows [4], which increases turbulence and promotes more complete combustion. The CRZ also leads to the formation of highly strained diffusion reaction layers with reduced flame temperatures and, consequently, NO<sub>x</sub> emissions [5, 6]. By integrating these features, the retrofit provides a robust solution for enabling hydrogen as a clean and efficient energy source in gas turbines. In this work, simultaneous 1D Raman and OH-LIF spectroscopy were applied to investigate the structure and stabilization mechanisms of a lifted hydrogen flame in a dual-swirl burner [7, 8]. The study provides a quantitative analysis of the flame's spatial profiles, temperature distribution, and mixture fraction behavior, contributing to a deeper understanding of hydrogen combustion dynamics.

\*zeinab.hadi@kaust.edu.sa

### III. Experimental Methods

The Raman instrument used in this work is analogous to that presented in [9]. Three Nd:YAG lasers are combined and sent through a 3-leg pulse stretcher, resulting in a 0.85 J pulse stretched over 500 ns. A 750 mm focal length spherical lens focuses the temporally stretched laser beams to the measurement volume. A pair of 6-inch diameter achromatic lenses (f/#2 and f/#4) relays the Raman signal to the focal plane where a mechanical shutter, providing a 330  $\mu$ s exposure time, is placed. The shutter consists of a Stanford Research Systems #SR540 optical chopper running at 50 Hz, equipped with a modified Thorlabs #MC1F6P10 chopper blade with a single 6-degree slot. A Sigma 135 mm, f/#1.8 lens camera lens, collimates the Raman signal and directs it through a broadband polarized cube-beam splitter. The vertical component of the signal, containing the majority of the Raman signal, goes through an optical shutter consisting of a large-aperture (40 mm) Pockels cell and two cross-oriented polarizers. Combined with the mechanical shutter, it results in an effective exposure of 0.98  $\mu$ s with a contrast ratio of 350 at the central region of our probe volume (2 mm range), which removes any chemiluminescence from the H<sub>2</sub> flames investigated here. A dichroic mirror (Semrock FF538-FD102-t3-55x55-EB) separates the Rayleigh scattering and the Raman signals. The Raman signal goes through a custom-built, low-resolution spectrometer consisting of a bandpass filter (Semrock, FF01-632/148-50), a notch filter (Edmund, #86-130), and a volume phase holographic transmission grating with 900 lines/mm (Wasatch Photonics). The spectrally dispersed signal is then focused onto another low-noise mode EMCCD camera using a 105 mm focal length, f/#1.4 Nikon lens. The Raman EMCCD camera is operated in a slow-readout ( $\approx$  18 ms) CCD mode to improve the signal-to-noise ratio.

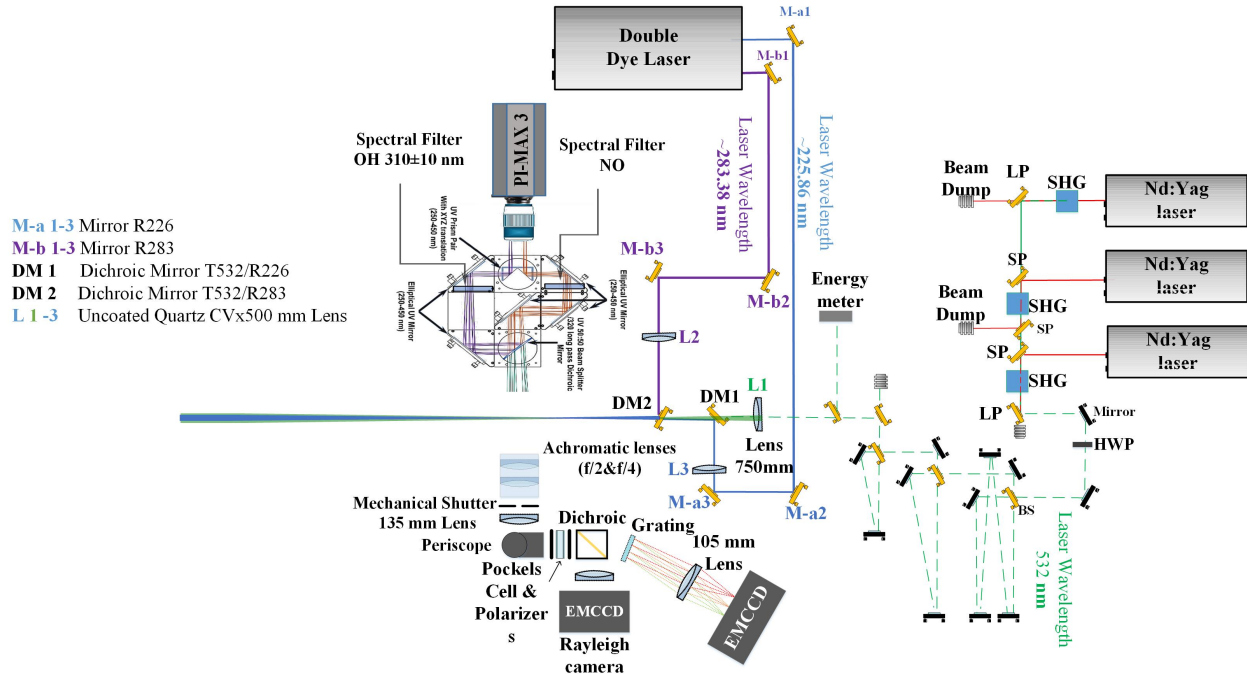


**Fig. 1 Schematic diagram of the experimental setup.**

Figure 1 shows a schematic of the combined Raman and dual LIF instrument used in this work for simultaneous measurements of OH and NO radicals provided by LIF measurements along with temperature and major species provided by the Raman measurements. However, the NO measurements will be discussed in future publications. The OH radical was excited using its  $Q_1(6)$  transition of the (1,0) band in the  $A^2\Sigma^+ \leftarrow X^2$  system at 283.37 nm. A tunable dual dye laser (Sirah Lasers PSCAN G24) operated at 10 Hz provided the excitation source with approximately 11 mJ/pulse for OH. Measurements in the product region of a flat-flame burner show that for energy greater than 5 mJ/pulse the OH-LIF intensity is in the partially saturated regime and nearly independent of the laser energy where a fluctuation of  $\sim 10\%$  in the laser energy results in  $< 2\%$  change in the signal as shown in Fig. 2. An identical optical setup to the one described by Boyette *et al.* in [10] was also used to obtain OH-PLIF images of the flame.

The hybrid matrix inversion approach [11] is used to extract the temperature and major species measurements from the Raman data. For the quantification OH concentrations from OH-LIF measurements, the following expression is

used:

$$S_{\text{OH}} = C_{\text{OH}} \times f_b(T) \times \frac{X_{\text{OH}}}{T}$$

where  $S_{\text{OH}}$  is the measured LIF signal,  $C_{\text{OH}}$  is an empirically determined calibration factor,  $T$  is the temperature deduced from the Raman measurements,  $f_b(T)$  is the Boltzmann distribution, and  $X_{\text{OH}}$  is the OH mole fraction. Quenching effects are neglected since the measurements are taken in the partially saturated regime, which allows the assumption of OH mole fraction being independent of the composition of the collisional bath.

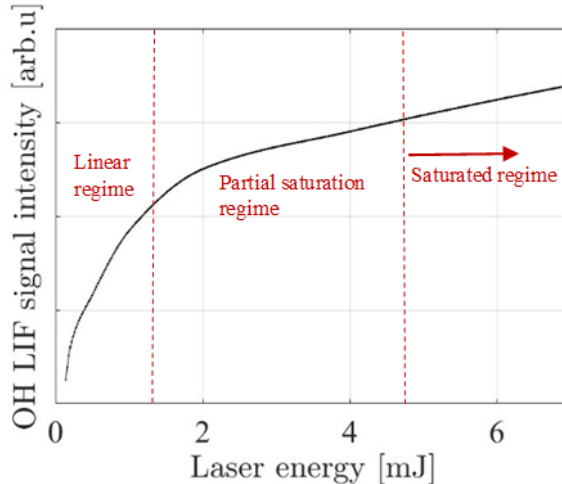


**Fig. 2 OH-LIF intensity as a function of the laser energy highlighting the OH-LIF saturation regime.**

Measurements in non-reactive air and N<sub>2</sub>/H<sub>2</sub> mixtures and in a series of H<sub>2</sub>/air flames stabilized over a McKenna burner, with equivalence ratios ranging from 0.9 to 1.8, provided the needed calibration coefficients and showed that the mean OH measurements are within 3% of the predicted molar fractions based on Chemkin calculations.

Experiments were performed using an updated version of the HYYLON (Hydrogen LOw NOx) injector studied in [12, 13]. It consists of a H<sub>2</sub>/air dual-swirl coaxial injector, where H<sub>2</sub> is injected through a central tube and air through an annular passage. The new version of the injector features a radial-to-axial swirling vane in the air channel and beveled lips with an inverted conical design for the H<sub>2</sub> injector, similar to the configuration described in [5] and depicted in Fig. 3.

The air swirler achieves a swirl number of  $S_e = 0.9$ , calculated based on geometric parameters, while the inner swirl number is estimated at  $S_i = 0.6$ . These swirl levels are given at the outlet of the swirlers. Both swirling flows rotate in a clockwise direction. The central H<sub>2</sub> channel has an internal diameter of  $d_i = 6$  mm, and the annular air channel has an external diameter of  $d_e = 18$  mm. The central tube begins with an external diameter of  $d_{ie0} = 10$  mm and expands radially to  $d_{ie} = 13$  mm over a length of  $y_0 = 1.5$  mm before the outlet of the H<sub>2</sub> tube. The outlet of the H<sub>2</sub> tube is recessed by  $y_i = 4.3$  mm relative to the outlet of the annular air channel.

Downstream of the injector, a square combustion chamber was installed. The chamber measures 145 mm in length and 78 mm in width. At the top of the chamber, a converging nozzle transitions from a square to a round section with a contraction ratio of 0.51. This design prevents dilution of the burnt gases in the chamber by outside air drawn into the combustor. The burner also features quartz windows for signal collection and metal plates with ~ 4 mm diameter holes featuring 1.2 mm chamfer at 7 axial locations to allow the laser beams to pass through the combustion chamber as shown in Fig. 4 to minimize unwanted scattering. 1D Raman/OH-LIF was applied to a lifted flame. The measurements allow analyzing the mean and instantaneous flame structure and temperature in physical (radial profiles) or mixture fraction spaces.

The time averaged OH\* image of the flame investigated in this experiment is shown in Fig. 5 where the flame is lifted above the injector lips. The dashed horizontal lines represent the heights at which 1D Raman and LIF data were acquired. The operating conditions of the flame are given in Table 1.

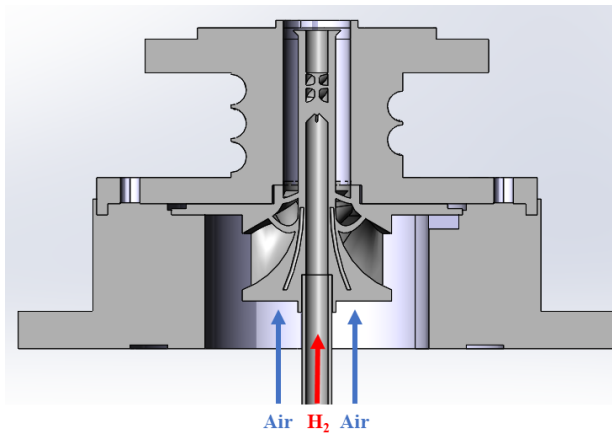


**Fig. 3** Dual swirl  $\text{H}_2/\text{air}$  burner.

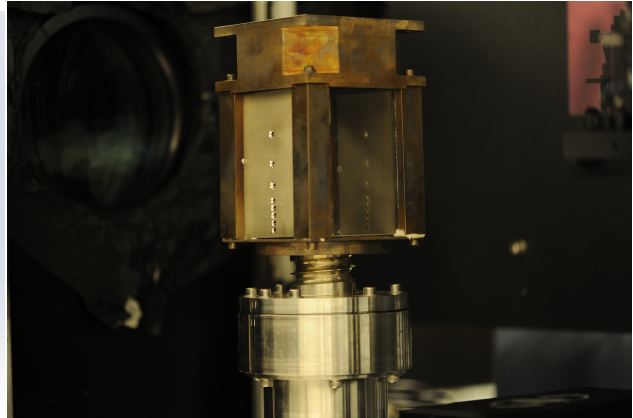


**Fig. 4** Burner side walls with drilled holes for laser diagnostics.

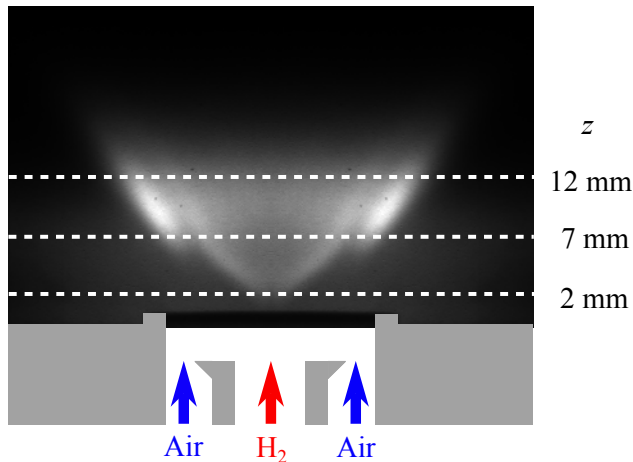


**Fig. 5** Time averaged  $\text{OH}^*$  image of the lifted flame  $L$  investigated.

**Table 1** Operating conditions for flame  $L$ .

$\dot{V}_{\text{air}}$	$\dot{V}_{\text{H}_2}$	$\Phi$	$P_{\text{th}}$	$u_{\text{air}}$	$u_{\text{H}_2}$	$\text{Re}_{\text{air}}$	$\text{Re}_{\text{H}_2}$
sL/min	sL/min		kW	m/s	m/s		
170	30	0.42	5.0	23.3	17.7	7460	964

#### IV. Results and Discussion

The measured mean profiles of molar fractions of oxygen  $X_{\text{O}_2}$ , hydrogen  $X_{\text{H}_2}$ , and of temperature  $T$  are shown in Fig. 6. The dashed lines, denoting the location of the peak of OH, show how the flame spreads axially from the bottom at  $z = 2 \text{ mm}$  to  $z = 12 \text{ mm}$ . Figures 7(a) and 7(b) show the mean spatial OH profiles at  $z = 7 \text{ mm}$  and  $z = 12 \text{ mm}$ , respectively. The locations of OH peaks in Fig. 7 correspond roughly to the peaks of temperature denoted by the dashed lines. Near the centerline for  $z = 7$  and  $12 \text{ mm}$ , the high temperature is close to the adiabatic value at the global equivalence ratio ( $T_{\text{ad}} \approx 1472 \text{ K}$ ), the  $\text{O}_2$  molar fraction is close to the value at the global equivalence ratio ( $X_{\text{O}_2} \approx 0.122$ ) and the absence of  $\text{H}_2$  confirms the presence of a CRZ in which burnt gases recirculate. At the right side of the radial profiles, an outer recirculating zone (ORZ) is detected, featuring a lower temperature and higher  $\text{O}_2$

molar fraction probably due to dilution by the jet of fresh air. The profiles of O<sub>2</sub> and H<sub>2</sub> molar fractions show the radial spreading of the central H<sub>2</sub> and external air jets, both swirled, progressively pre-heated increasing the axial distance from the injector outlet. At the bottom axial location ( $z = 2$  mm), Fig. 5 shows that the flame front is located near the centerline, at the interface between the H<sub>2</sub> jet and the burnt gases recirculated in the CRZ. No reaction front is identified at the interface as shown in Fig. 7(a) between the H<sub>2</sub> and the air jets, due to the high velocities at this location, preventing the external flame front from propagating to the central injector lips, as highlighted by Marragou *et al.* [12].

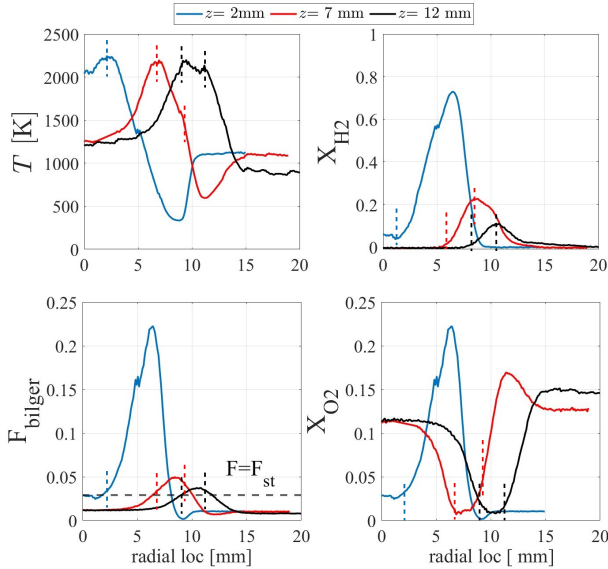


**Fig. 6 Radial profiles of molar fractions of O<sub>2</sub> and H<sub>2</sub>, temperature, and Bilger mixture fraction at  $z = 2$  mm,  $z = 7$  mm and  $z = 12$  mm (see Fig. 5). The location of the peaks of OH are denoted with dashed lines on the profiles.**

Further downstream at  $z = 7$  mm, a second OH peak is identified. The inner one is still located at the interface between the H<sub>2</sub> jet and the CRZ and a second outer one now appears at the interface between the H<sub>2</sub> and the air jets. The flame, however, only produces a small trace on the mean temperature profile. This point is further discussed below. At  $z = 12$  mm, these two peaks are more evident on the mean temperature profiles. The radial profiles of H<sub>2</sub> molar fraction further highlight the rapid mixing of H<sub>2</sub> with air.

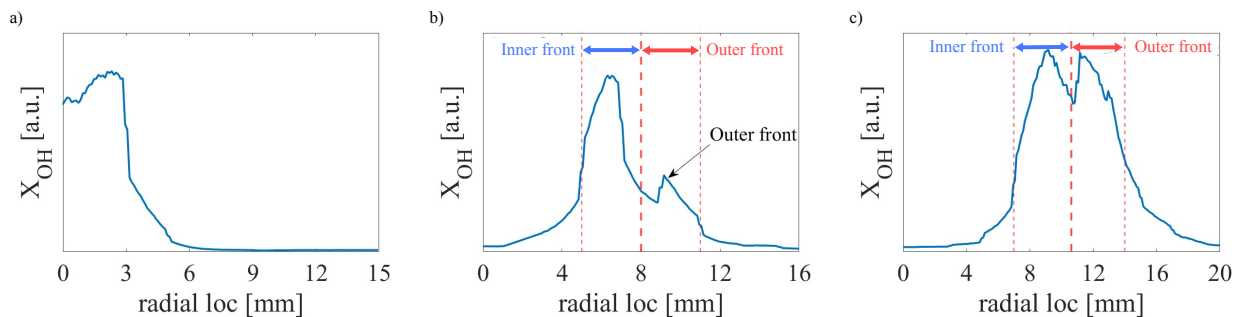


**Fig. 7 Mean spatial OH profiles at (a)  $z = 2$  mm, (b)  $z = 7$  mm, and (c)  $z = 12$  mm.**

To quantitatively understand the separate burning zones, the probability distribution function (PDF) of the temperature and Bilger mixture fraction at the spatial strips of each of the two flame fronts (inner and outer) is computed in Figs. 8, and 9 for  $z = 7$  and 12 mm respectively. The temperature at the outer front at  $z = 7$  mm shows a bimodal distribution in Fig. 8(b), heavily concentrated in the colder temperature zones. The inner flame front, on the other hand, shows in Fig. 8(a) a broad unimodal temperature peak centered around  $T \approx 1950$  K, consistent with stable combustion.

Consequently, the Bilger mixture fraction in Fig. 8 is broader at the bimodal outer front than in the unimodal inner front.

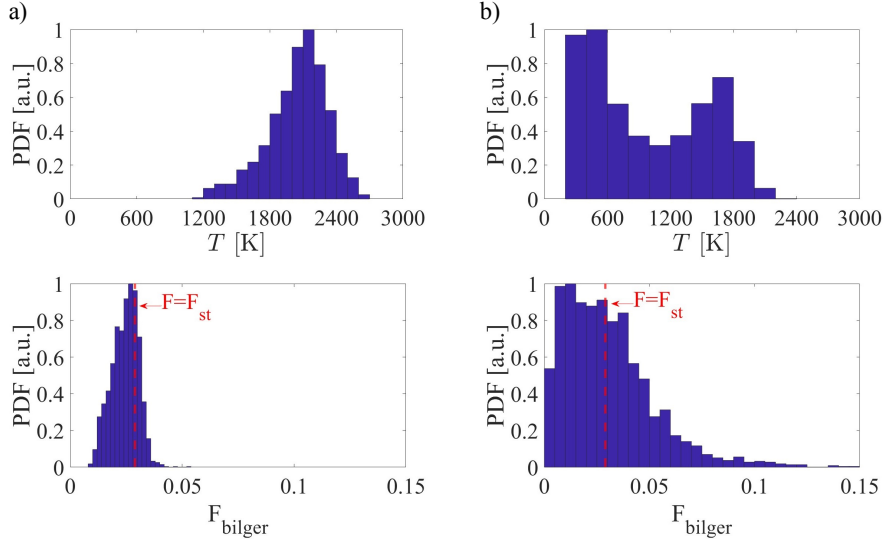


**Fig. 8 PDF of the temperature  $T$  and Bilger mixture fraction  $F_{\text{bilger}}$  at  $z = 7 \text{ mm}$  for the inner (a) and outer (b) reaction front.**

Further downstream, at  $z = 12 \text{ mm}$  in Fig. 9, the bimodality for the external flame front disappears, and both fronts exhibit broader but more uniform temperature and Bilger mixture fraction distributions, reflecting the continuous presence of the flame. The higher temperatures  $\sim 2100 \text{ K}$  in the outer front at  $z = 12 \text{ mm}$  are where the samples are mainly populated, showing that the flame is dominantly burning in diffusion mode.

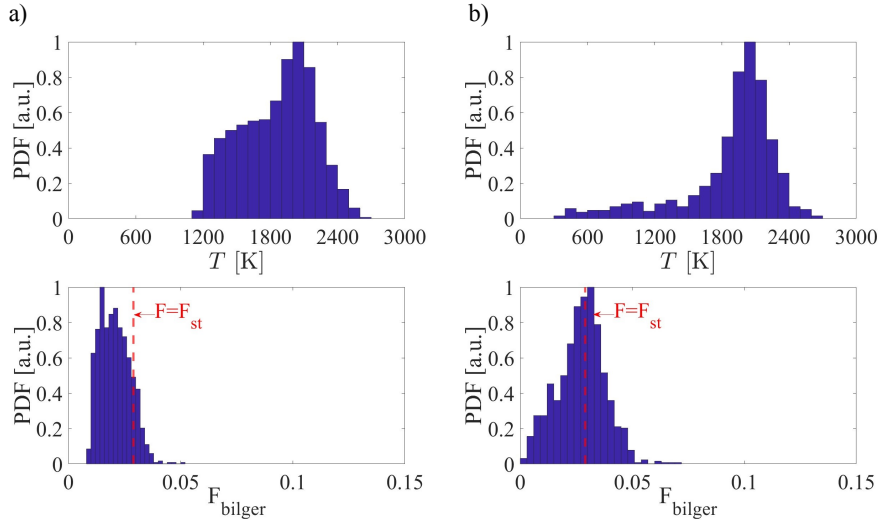


**Fig. 9 PDF of the temperature  $T$  and Bilger mixture fraction  $F_{\text{bilger}}$  at  $z = 12 \text{ mm}$  for the inner (a) and outer (b) reaction front.**

High-speed OH-PLIF images of the flame, shown in Fig. 10 clarify the bimodal behavior observed at  $z = 7 \text{ mm}$ . The temporal series of OH-PLIF images in Fig. 10 captures the intermittent behavior of the outer reaction front. Variations in flame brightness over successive frames reveal oscillatory burning and a quenching event of the external reaction front. At  $z = 7 \text{ mm}$ , the flame is intermittently present, while it is always present at  $z = 12 \text{ mm}$ . The bottom of the external reaction front is an edge flame, propagating upstream when the flow velocity conditions are favorable and going back downstream when a positive fluctuation of the velocity and/or strain rate occurs. These observations support the

high turbulence level and strain rate inferred from the scatter plots and molar fraction profiles. This is especially clear when comparing the images at  $t_0 + 0.1$  ms and at  $t_0 + 0.3$  ms. The high turbulence affects the flame stabilization and can cause this external front to move up and down along the flame. Consequently, the flame penetrates intermittently the measurement volume, leading to the two-branch behavior observed in Fig. 12 for  $z = 7$  mm, and which disappears at  $z = 12$  mm, height for which the flame is continuously present in the measurement volume. Qualitatively, there is agreement between direct flame visualizations and the distributions of the molar fractions and temperature in the scatter plots.

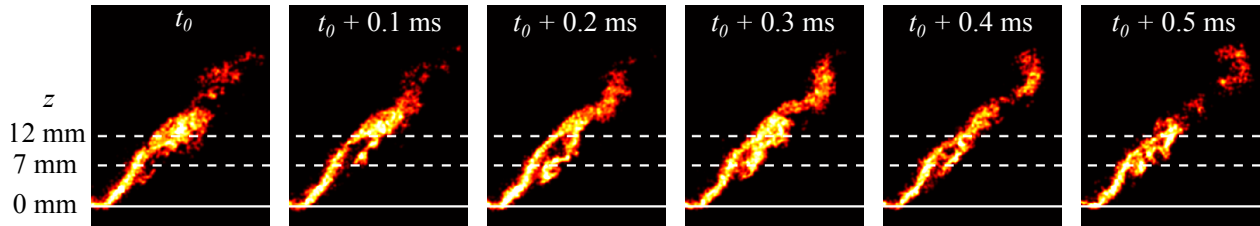


**Fig. 10 Illustration of the flame dynamics from high-speed OH-PLIF imaging at different instants.**

Figure 11 shows the molar fractions of oxygen  $X_{O2}$  and hydrogen  $X_{H2}$ , and the temperature in Bilger mixture fraction  $F_{Bilger}$  space at  $z = 2$  mm. At this location, the hot exhaust gases recirculating in the CRZ lead to a significant scatter in the instantaneous measured temperature, as seen in Fig. 11. The peak of the mean temperature at this axial location shown in Fig. 11(a) is  $T \sim 2320$  K at  $F_{Bilger} \approx F_{st}$ , where  $F_{st}$  is the stoichiometric value of the Bilger mixture fraction. The mixture fraction range is wide (between 0.0 to 0.6) which is expected due to the presence of almost pure air and hydrogen fresh gases (due to the proximity to the separate H<sub>2</sub>/air injection holes) and burnt gases.

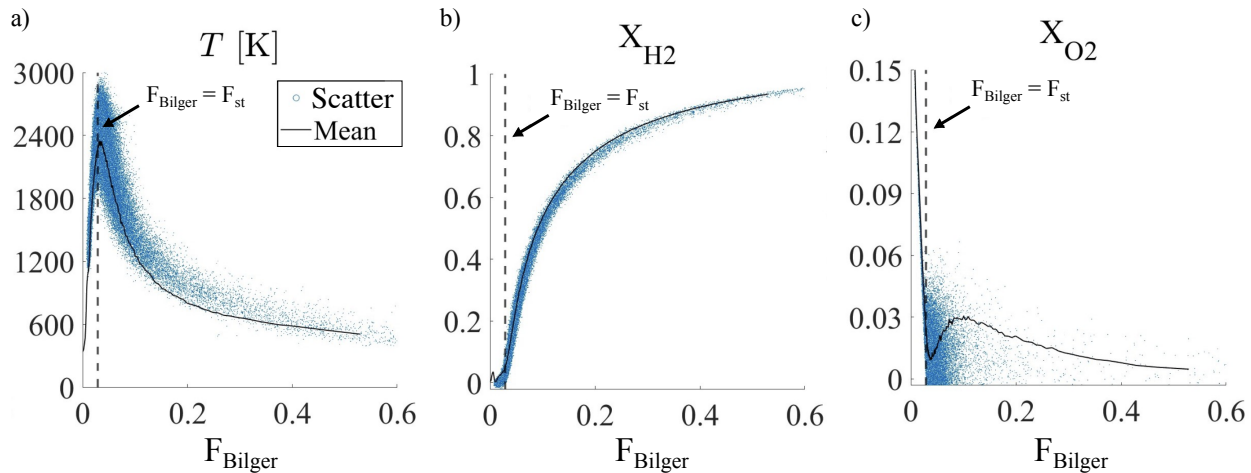


**Fig. 11 Temperature (a) and molar fractions of H<sub>2</sub> (b) and O<sub>2</sub> (c) measurements at  $z = 2$  mm plotted against the Bilger mixture fraction  $F_{Bilger}$ .**

The OH\* image in Fig. 5 shows a burning zone at the external boundaries at  $z = 7$  mm and  $z = 12$  mm. Further examination of OH radial profiles is needed to explain this. The OH profiles in Fig. 7, in agreement with the OH\* image, show two separate peaks corresponding to two different reaction fronts, the inner front and the outer front. To study the nature and the behavior of each of these fronts separately, the molar fractions of O<sub>2</sub> and H<sub>2</sub> as well as the temperature in the Bilger mixture fraction space at each front are investigated in Figs. 12 and 13. The two reaction fronts are split spatially as shown in Figs. 7(a) and 7(b) for  $z = 7$  and 12 mm respectively. At axial location  $z = 7$  mm in Fig. 7(a), two well separated reaction fronts are distinguished. However, further downstream at  $z = 12$  mm in Fig. 7(b) these fronts come closer and almost merge.

Figures 12 and 13 investigate the behaviors of two flame fronts separately by analyzing the molar composition and temperature in each section/front.

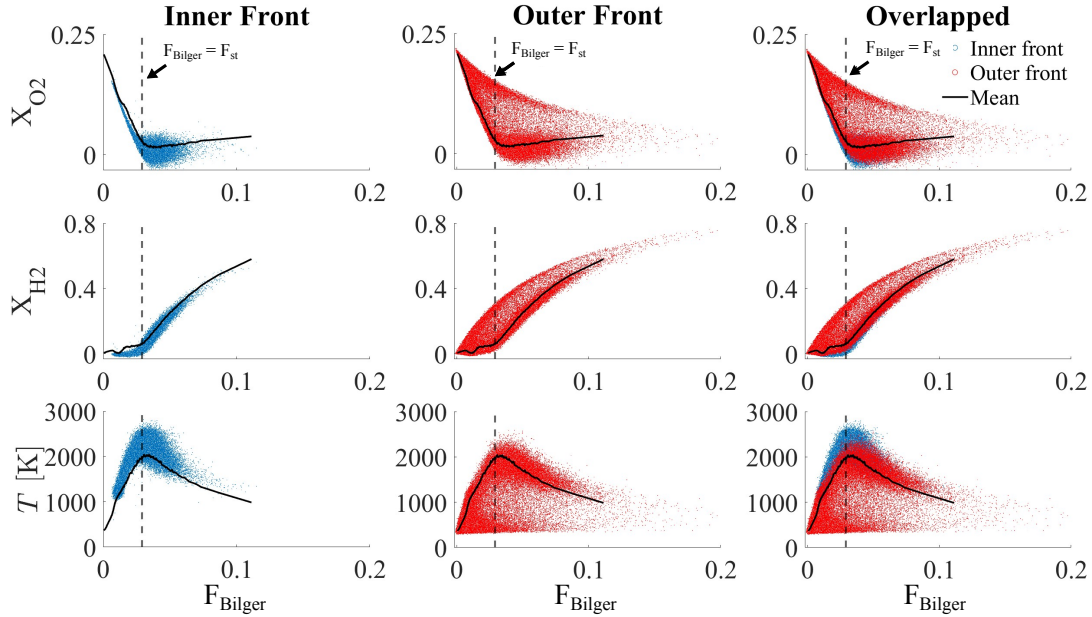


**Fig. 12 Molar fractions of  $O_2$ ,  $H_2$ , and temperature measurements in the flame at  $z = 7$  mm**

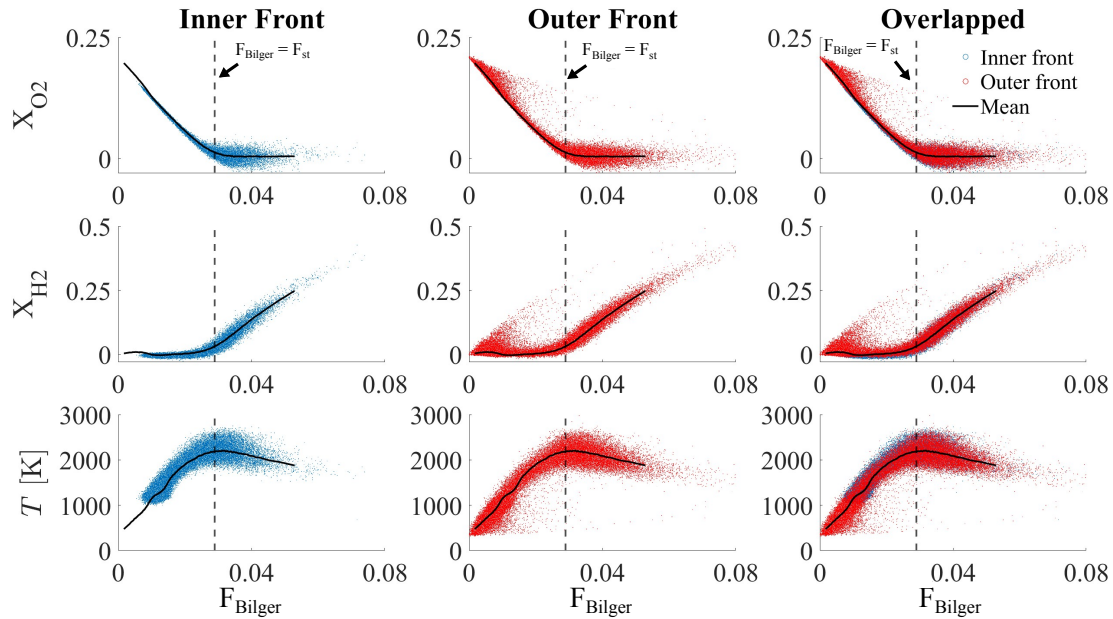


**Fig. 13 Molar fractions of  $O_2$ ,  $H_2$  and temperature measurements in the flame at  $z = 12$  mm**

It appears in Fig. 12 that the inner front and the outer front at  $z = 7$  mm burn differently. The inner front (blue) portrays a classical diffusion flame behavior where the scatter plot of the temperature shows an expected diffusion-like slope. However, the outer front (red) shows a bimodal behavior consistent with what is observed in Fig. 8. One branch, (lower in  $O_2$  and  $H_2$ , higher in temperature), matches well the non-premixed flame structure observed in the inner front, except for a lower mean peak temperature, associated to the higher strain rate expected in the outer location. The other branch is characterized by high values of  $O_2$  and  $H_2$  and low values of temperature, indicating a non-reacting mixing region. The presence of values intermediate between these two branches suggests strong turbulence/chemistry interaction in this region. The flame further downstream at  $z = 12$  mm in Fig. 13 doesn't exhibit the same behavior

as that at  $z = 7$  mm. The inner and outer front exhibit almost an identical behavior with a match to the mean molar fractions of H<sub>2</sub> and O<sub>2</sub>.

## V. Conclusions

A lifted H<sub>2</sub>/air flame stabilized above a dual swirl injector was investigated. High fidelity measured concentrations of major species, OH, and temperature using simultaneous 1D Raman/OH-LIF spectroscopy were presented. The findings can be summarized as follows:

- The flame stabilizes through a dual-reaction front mechanism: an inner diffusion reaction front at the interface between the central H<sub>2</sub> jet and the recirculating hot burnt gases and an outer reaction front fed by a mixture of fresh air and H<sub>2</sub>.
- The outer reaction front exhibits high intermittency, attributed to the elevated turbulence and strain rates in its vicinity. The edge flame at the lower extremity of this reaction front intermittently propagates upstream and downstream in the flow, depending on instantaneous flow conditions.
- The presence of intermittent flames at intermediate heights is corroborated by the structure of the scatter plots of the molar fractions of O<sub>2</sub> and H<sub>2</sub> and temperature in the fraction space of the Bilger mixture. For the outer reaction front, the data reveal a two-branch structure, one corresponding to cold flow mixing and the other to a diffusion reaction front. Further downstream and for the inner reaction front, the structure transitions to a classical pattern, indicating the continuous presence of a reaction front within the measurement volume.
- This behavior is further corroborated by the bi-modal distribution of the probability density function of the temperature at the outer reaction front at intermediate heights. This bimodality disappears downstream and for the inner reaction front, indicating a stable reaction front.
- Simultaneous Raman and LIF measurements provide a high precision data set that is crucial to understand the fundamental properties of such flames, validate numerical models, and inform the design of low-NO<sub>x</sub> hydrogen combustion systems.

## VI. Acknowledgements

The research reported in this publication was supported by the King Abdullah University of Science and Technology (KAUST) through a Competitive Research Grant (grant number URF/1/5039–01–01). This project received also funding from European Union Horizon ERC SELECT-H (grant 101097984).

## References

- [1] Antunes Gomes, M., Mikalsen, R., and Roskilly, A., “An investigation of hydrogen-fuelled HCCI engine performance and operation,” *International Journal of Hydrogen Energy*, 2008, pp. 5823–5828.
- [2] Richard, S., Viguer, C., Marragou, S., and Schuller, T., *Device for injecting dihydrogen and air (WO Patent No WO2023057722A1)*, Institut National de la Propriété Industrielle, 2023.
- [3] Syred, N., and Beer, J., “Combustion in swirling flows: a review,” *Combustion and flame*, Vol. 23, No. 2, 1974, pp. 143–201.
- [4] Marragou, S., Guiberti, T., Poinsot, T., and Schuller, T., “Near-field mixing in a coaxial dual swirled injector,” *Flow Turbulence and Combustion*, 2024.
- [5] Magnes, H., Vilesipy, M., Selle, L., Poinsot, T., and Schuller, T., “Interplay Between Unburned Emissions and NOx Emissions From a Dual Swirl Hydrogen Air Injector,” *ASME Journal of Engineering for Gas Turbines and Power*, Vol. 147, No. 6, 2025, p. 061013.
- [6] Vilesipy, M., Aniello, A., Laera, D., Poinsot, T., Schuller, T., and Selle, L., “Analysis of the origin of NOx emissions in non premixed dual swirl hydrogen flames,” *Combustion and Flame*, 2025. Accepted.
- [7] Aniello, A., Laera, D., Marragou, S., Magnes, H., Selle, L., Schuller, T., and Poinsot, T., “Experimental and numerical investigation of two flame stabilization regimes observed in a dual swirl H<sub>2</sub>-air coaxial injector,” *Combustion and flame*, Vol. 249, 2023, p. 112595.
- [8] Marragou, S., Magnes, H., Poinsot, T., Selle, L., and Schuller, T., “Stabilization regimes and pollutant emissions from a dual fuel CH<sub>4</sub>/H<sub>2</sub> and dual swirl low NO<sub>x</sub> burner,” *International Journal of Hydrogen Energy*, Vol. 47, No. 44, 2022, pp. 19275–19288.

- [9] Tang, H., Ezendeava, D., and Magnotti, G., "Simultaneous measurements of NH<sub>2</sub> and major species and temperature with a novel excitation scheme in ammonia combustion at atmospheric pressure," *Combustion and Flame*, Vol. 250, 2023, p. 112639.
- [10] Boyette, W. R., Guiberti, T. F., Elbaz, A. M., and Roberts, W. L., "High-Speed Imaging of Turbulent Nonpremixed Syngas Flames at Elevated Pressures," *Proceedings of THMT-18: Turbulence Heat and Mass Transfer 9 – Ninth International Symposium on Turbulence, Heat and Mass Transfer*, 2018.
- [11] Fuest, F., Barlow, R., Geyer, D., Seffrin, F., and Dreizler, A., "A hybrid method for data evaluation in 1-D Raman spectroscopy," *Proceedings of the Combustion Institute*, Vol. 33, No. 1, 2011, pp. 815–822.
- [12] Marragou, S., Magne, H., Aniello, A., Guiberti, T., Selle, L., Poinsot, T., and Schuller, T., "Modeling of H<sub>2</sub>/air flame stabilization regime above coaxial dual swirl injectors," *Combustion and Flame*, Vol. 255, 2023, p. 112908.
- [13] Marragou, S., Guiberti, T., Poinsot, T., and Schuller, T., "Near-field mixing in a coaxial dual swirled injector," *Flow, Turbulence and Combustion*, Vol. In Press, 2024.